Co- and Ni-Free O3-Type Layered NaFe$_{0.45}$Mn$_{0.5}$Ti$_{0.05}$O$_2$ Cathode for Sodium-Ion Batteries

Nagu Ajmeera,* Vinoth Kumar Jayaraman, and Deepak Kumar

The rising costs of cobalt and nickel, alongside mounting environmental concerns, have spurred intensive research into alternative battery chemistries that eliminate these critical elements. This shift aligns with the broader industry push toward low-cost, sustainable materials that can rival the performance of lithium–iron–phosphate (LFP) systems. In this context, the present work introduces a layered oxide cathode composition, NaFe$_{0.45}$Mn$_{0.5}$Ti$_{0.05}$O$_2$ (NFMTO), which delivers high specific capacity and enhanced cycling stability. The substitution of Ti^{4+} into the Fe/Mn lattice effectively modifies the transition metal–oxygen (TM-O) layer spacing, thereby improving structural stability during cycling. As a result, the NFMTO cathode exhibits an initial discharge capacity of 125 mAh g^{-1} at 0.1C (2.0–4.2 V vs. Na$^+$/Na) and retains 78.4% of its capacity after 50 cycles. Additionally, it delivers 118 mAh g^{-1} with 70% capacity retention over 200 cycles in a voltage window of 2.0–4.0 V. The full-cell performance of NFMTO is evaluated in a pouch cell configuration using hard carbon as the anode, further demonstrating its practical viability. The assembled pouch cell delivered an initial discharge capacity of 103 mAh g^{-1} at 0.05C (2.0–4.2 V) and retained 90% of its capacity after 10 cycles.

1. Introduction

The rising global demand for efficient and cost-effective energy storage solutions has positioned battery technologies at the forefront of scientific and industrial innovation. While lithium-ion batteries (LIBs) currently dominate the market, concerns regarding the limited availability and increasing cost of lithium, coupled with safety considerations, have spurred intensive research into promising alternatives. Among these, sodium-ion batteries (SIBs) have emerged as a particularly compelling candidate, leveraging the Earth's abundant and inexpensive sodium resources, exhibiting inherent safety advantages, and sharing fundamental electrochemical similarities with their lithium counterparts.[1–7]

This confluence of factors has propelled SIB research into a phase of rapid expansion within the battery sector. A critical factor in realizing the full potential of SIB technology lies in the careful selection and strategic engineering of cathode materials, which fundamentally govern the electrochemical performance of these energy storage systems. SIB cathodes are typically classified into three main categories: layered TM oxides, polyanionic compounds, and Prussian blue analogs.[8,9] Among these, layered TM oxides (Na$_x$TMO$_2$) have garnered significant attention due to

their relatively simple synthesis, high theoretical capacities, and the compositional flexibility afforded by incorporating a variety of TMs into their structural framework.

Layered materials are characterized by MO$_2$ slabs composed of edge-sharing MO$_6$ octahedra, with sodium ions occupying either octahedral (O-type) or trigonal prismatic (P-type) sites.[10] Structural distinctions further arise based on sodium content and oxygen stacking sequences, leading to their classification into O3 ($0.9 < x < 1$), P2 ($0.6 < x < 0.8$), and P3 ($0.5 < x < 0.6$) types, which correspond to ABCABC, ABBA, and ABBCCA oxygen stacking, respectively.[11] While P2- and P3-type oxides exhibit certain electrochemical advantages, their inherent sodium deficiency and challenges in full-cell integration often limit their practical applications. In contrast, O3-type layered oxides offer the benefits of higher sodium content and better compatibility with conventional full-cell configurations.[12–15] However, many O3-type cathodes, such as NaFe$_{0.5}$Co$_{0.5}$O$_2$, NaNi$_{1/3}$Mn$_{1/3}$Co$_{1/3}$O$_2$, NaNi$_{0.32}$Co$_{0.15}$Fe$_{0.13}$Mn$_{0.40}$O$_2$, and NaMn$_{0.25}$Fe$_{0.25}$Co$_{0.25}$Ni$_{0.25}$O$_2$, rely on cobalt and nickel, which are scarce and expensive elements.[16–18]

Consequently, the design and development of robust O3-type cathode materials composed of earth-abundant elements are essential for advancing sustainable and high-performance SIBs. Addressing this critical need, the present study introduces a low-cost, cobalt- and nickel-free O3-type layered oxide cathode, NaFe$_{0.45}$Mn$_{0.5}$Ti$_{0.05}$O$_2$, engineered to enhance both specific capacity and cycling stability. By strategically incorporating a small amount of Ti^{4+} into the Fe/Mn oxide framework, this work aims to improve the structural stability and overall electrochemical performance of the material. The beneficial effects of Ti^{4+} substitution have been extensively investigated in various sodium-layered oxides and are well-documented in the literature.[19–23] The high oxidation state

N. Ajmeera, V. K. Jayaraman, D. Kumar
Council of Scientific and Industrial Research
Central Electrochemical Research Institute-Chennai Unit
CSIR Madras Complex
Taramani, Chennai 600113, India
E-mail: ajmeeranagu1@gmail.com

D. Kumar
Academy of Scientific and Innovative Research (AcSIR)
Ghaziabad 201002, India

of Ti^{4+}, combined with the strong Ti—O bond and the inherent structural robustness of TiO_2, significantly contributes to enhancing the overall structural integrity of the host material. Furthermore, TiO_2 possesses attributes such as wide availability, cost-effectiveness,

nontoxicity, and chemical stability, which make it particularly suitable for large-scale industrial applications.[24,25] The practical applicability of the developed material further substantiated through the successful fabrication and electrochemical evaluation of a pouch cell. To explicitly delineate the influence of Ti doping on capacity retention and long-term cycling behavior, the performance of $NaFe_{0.45}Mn_{0.5}Ti_{0.05}O_2$ (NFMTO)

is directly compared to that of its undoped counterpart, $NaFe_{0.5}Mn_{0.5}O_2$ (NFMO).

2. Results and Discussion

$NaFe_{0.5}Mn_{0.5}O_2$ and $NaFe_{0.45}Mn_{0.5}Ti_{0.05}O_2$ were synthesized using a solid-state method. The X-ray diffraction (XRD) patterns of the NFMO and NFMTO were acquired in the 2θ range of 10° to 80°, as depicted in **Figure 1**a,b, to obtain phase purity and other structural parameters. Both samples exhibited diffraction patterns consistent with a hexagonal lattice belonging to the $R\bar{3}m$
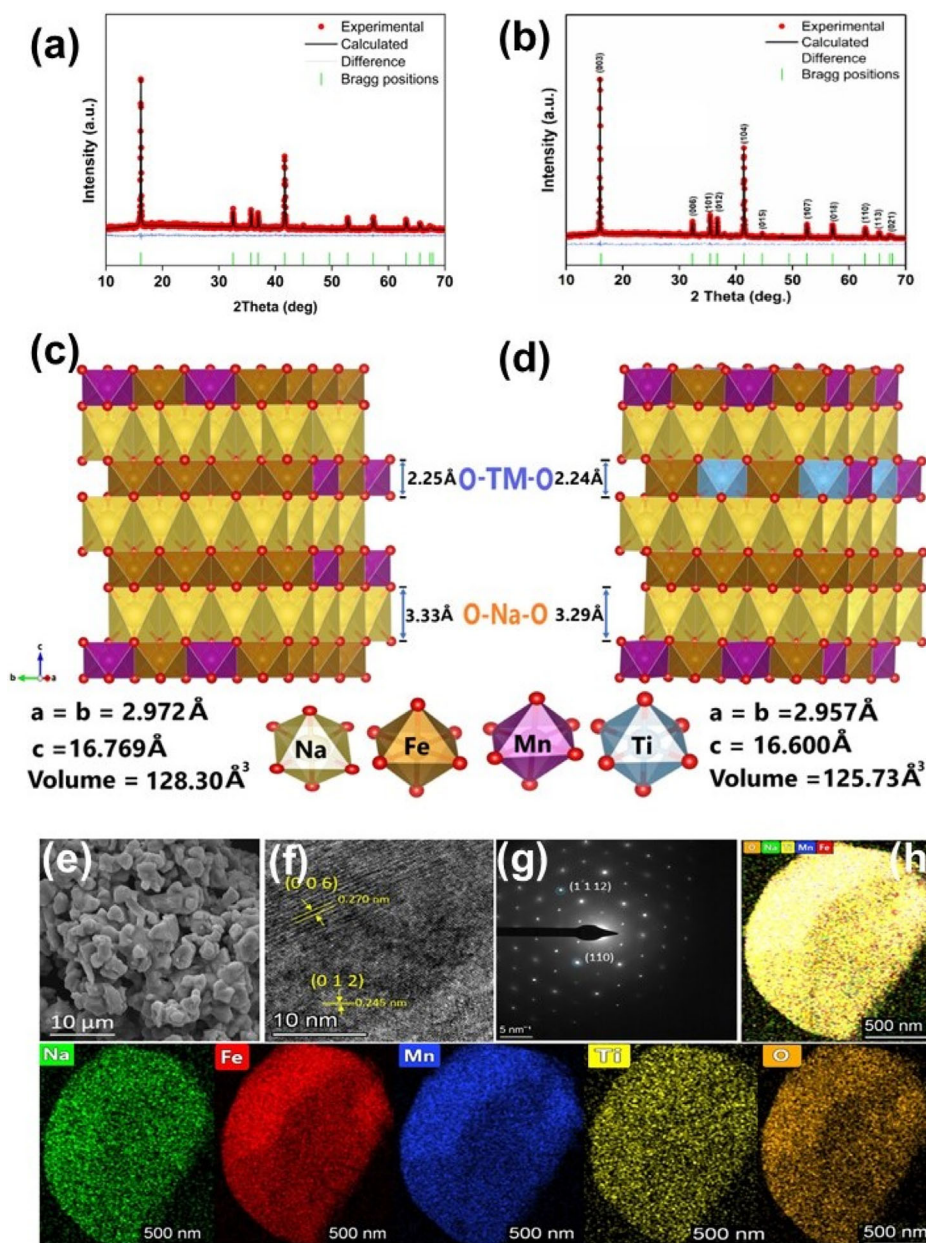

Figure 1. a,b) XRD diffraction patterns of NFMO and NFMTO and its rietveld refinement, c,d) crystal structures of the NFMO and NFMTO, e) FESEM, and f–h) HRTEM of NFMTO and its corresponding elemental mapping, respectively.

Batteries & Supercaps

Research Article
doi.org/10.1002/batt.202500498

**Chemistry
Europe**
European Chemical
Societies Publishing

space group, characteristic of an O3-type structure (ICDD 01-082−1495). The intensity ratio of (003)/(104) > 1.2 indicates that the samples are well-ordered structure.

Further, detailed structural analysis was carried out using Rietveld refinement of the XRD data to precisely determine the crystal structure parameters for both the pristine and Ti-doped samples. For NFMO, the refined lattice parameters were $a = b = 2.972(9)$ Å and $c = 16.769(2)$ Å, yielding a unit cell volume of 128.30 Å^3. Upon the incorporation of titanium to form NFMTO, a noticeable contraction of the hexagonal lattice was observed. The refined lattice parameters for the Ti-doped sample were $a = b = 2.957(1)$ Å and $c = 16.600(4)$ Å, resulting in a reduced unit cell volume of 125.73 Å^3.

Figure 1c,d illustrate the typical O3-type oxide structure. This structure features TM oxide layers (TMO$_2$, TM = Fe, Mn or/and Ti) composed of TMO$_6$ octahedra that share edges along the c-axis. Oxygen atoms exhibit cubic close-packed stacking in an ABCABC sequence with Na$^+$ occupying the octahedral sites between these layers.

Analysis of the refined structural parameters revealed a systematic decrease in interlayer distances and bond lengths. The sodium layer interlayer distance contracted from 3.331 Å in NFMO to 3.293 Å in NFMTO. Similarly, the transition metal (TM) layer interlayer distance decreased from 2.258 to 2.245 Å. Concurrently, the average metal–oxygen (TM—O) bond length slightly decreased from 2.0542 to 2.0434 Å, and the average sodium—oxygen (Na—O) bond length reduced from 2.3916 to 2.3703 Å. The observed lattice shrinkage and bond contraction are attributed to the substitution of smaller and more highly charged Ti^{4+} ions into the TM sites. The ionic radius of Ti^{4+} (0.605 Å) and Mn^{4+} (0.53 Å) are both smaller than that of Fe^{3+} (0.645 Å). This difference in ionic radii leads to a reduced thickness of the TM layer in the Ti-substituted material.[24,25]

Field emission scanning electron microscopy (FESEM) images of the NFMTO powder sample (Figure 1e) contains irregular shaped particles of size variations in between 2 and 6 μm. The high-resolution transmission electron microscopy (HRTEM) image of NFMTO (Figure 1f) clearly exhibits two sets of well-defined lattice fringes with measured d-spacings of 0.270 and 0.245 nm, which are indexed to the (006) and (012) crystallographic planes of the $R\bar{3}m$ phase, respectively. In the selected area electron diffraction (SAED) patterns as in Figure 1g, a typical hexagonal symmetry in the arrangement of metal atoms, which is associated with the O3-type structure. Identical observations have been reported for other O3-compositions such as Na$_{0.8}$Ni$_{0.6}$Sb$_{0.4}$O$_2$ cathode, and NaNi$_{0.4}$Mg$_{0.1}$Al$_{0.1}$Ti$_{0.3}$Sb$_{0.1}$O$_2$.[26,27] The TEM-energy dispersive X-ray mapping in Figure 1h depicts the uniform distribution of elements, including Na, Fe, Mn, Ti, and O.

X-ray photoelectron spectroscopy (XPS) was used to investigate the surface chemical states of the cathode, as shown in **Figure 2**. The Mn 2p spectra (Figure 2b,d) of both the samples were deconvoluted into four distinct peaks located at 654.3, 653.1, 642.7, and 641.7 eV, corresponding to Mn^{4+} 2p$_{1/2}$, Mn^{3+} 2p$_{1/2}$, Mn^{4+} 2p$_{3/2}$, and Mn^{3+} 2p$_{3/2}$, respectively. It is worth to note that the area of Mn^{4+} in NFMTO is increased by 2% in the peak fitting when compared to pristine compound, which implies that Mn^{4+} acts as structural stabilizer, in turn may enhance the structural stability. Similar improvements in structural stability have been reported in previous studies.[28–30]
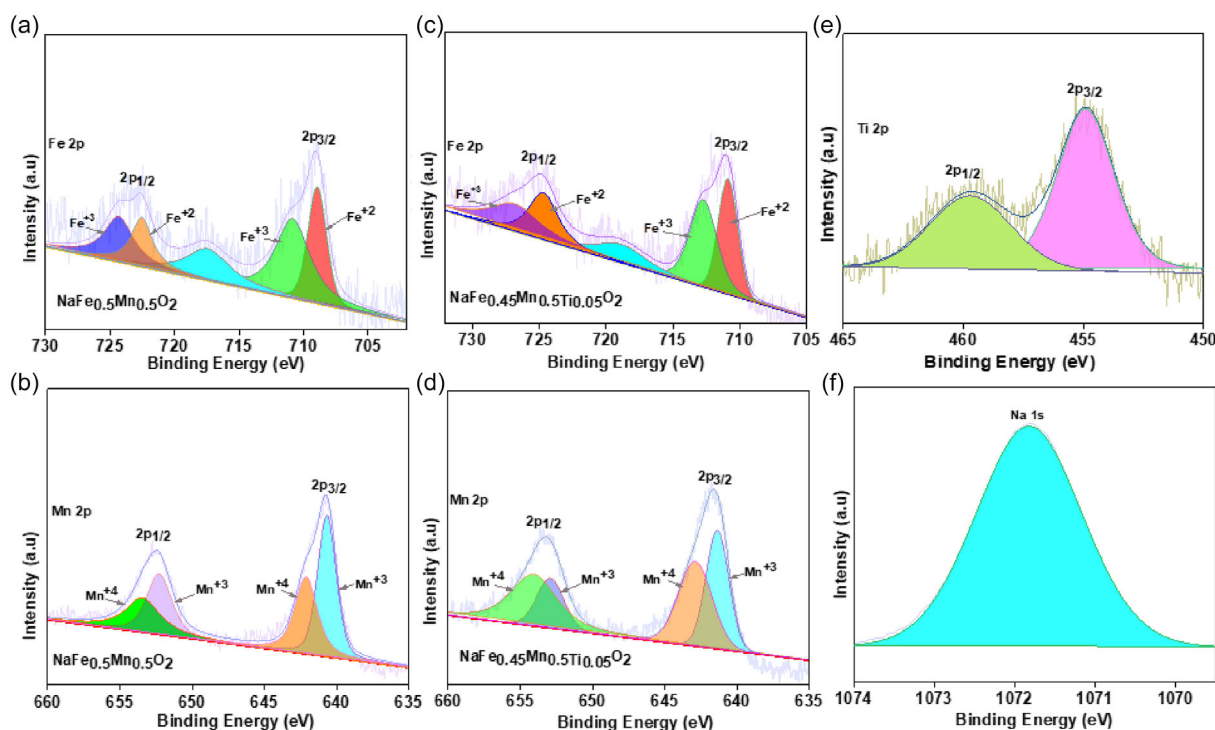

Figure 2. XPS spectra of a) Fe 2p, b) Mn 2p of NFMO, c) Fe 2p, d) Mn 2p, e) Ti 2p, and f) Na 1s of NFMTO.

Batteries & Supercaps

Research Article
doi.org/10.1002/batt.202500498

Chemistry Europe
European Chemical
Societies Publishing

Similarly, the Fe 2p spectra (Figure 2a,c) exhibit four prominent peaks at 724.9, 722.0, 711.3, and 709.5 eV, which are attributed to Fe^{3+} $2p_{1/2}$, Fe^{2+} $2p_{1/2}$, Fe^{3+} $2p_{3/2}$, and Fe^{2+} $2p_{3/2}$, respectively. In the case of the Ti 2p region (Figure 2e), a dominant peak at 458.4 eV confirms Ti^{4+}.

The cyclic voltammetry (CV) profiles of the pristine and Ti-doped cathodes were obtained in 2–4.2 V at the current of 0.1 mV s^{-1} as shown in **Figure 3**a,d. For the pristine NFMO two anodic peaks are observed at 2.62 and 4.02 V, which correspond to the oxidation of Mn^{3+}/Mn^{4+} and Fe^{3+}/Fe^{4+} redox couples, respectively. The cathodic peaks are found at 2.09 and 3.30 V, associated with the reduction of Mn^{4+}/Mn^{3+} and Fe^{4+}/Fe^{3+}, respectively.

In contrast, for the Ti-doped NFMTO sample, the anodic peaks shift to 2.54 and 4.00 V, indicating slight shifts in the oxidation potentials of Mn^{3+}/Mn^{4+} and Fe^{3+}/Fe^{4+} compared to the pristine material. The cathodic peaks for the Ti-doped cathode appear at 2.18 and 3.32 V, showing a similar shift in the reduction potentials. These results suggest that Ti doping has a notable influence in improving the redox behavior of the cathode material.[28]

To elucidate the initial electrochemical performance of the as-prepared NFMO and NFMTO samples, galvanostatic charge–discharge (GCD) profiles were acquired within a voltage window of 2.0–4.0 V versus Na$^+$/Na at a current rate of 0.1C as in Figure 3b,e. The pristine NFMO (Figure 3b) exhibited an initial discharge capacity of 128 mAh g^{-1}; however, subsequent cycling revealed substantial capacity degradation, indicative of poor structural stability. Conversely, the NFMTO electrode, presented in Figure 3e, delivered a slightly lower initial discharge capacity of 118 mAh g^{-1} but exhibited superior cycling stability. To further evaluate the cycling stability of the prepared cathodes at higher voltage, GCD testing was conducted in the voltage range of 2.0–4.2 V (vs. Na$^+$/Na) at a current rate of 0.1C.

Figure 3f, the NFMTO electrode achieved an initial discharge capacity of 125 mAh g^{-1} and retained 98 mAh g^{-1} after 50 cycles, corresponding to a capacity retention of 78.4%. Under identical conditions, the NFMO electrode retained only 30% of its initial capacity, thereby highlighting the superior structural and electrochemical stability of the NFMTO composition. This advantage was further confirmed by extended cycling experiments as shown in **Figure 4**, where NFMTO sustained approximately 70% of its initial discharge capacity after 200 cycles, compared to only 16% for NFMO. Such remarkable improvement in long-term performance highlights the critical role of Ti incorporation in stabilizing the layered structure and mitigating capacity fade.

The enhanced capacity retention in NFMTO can be attributed to multiple synergistic factors arising from Ti incorporation. The Ti—O bond energy (662 kJ mol^{-1}) is significantly higher than that of both Fe—O (409 kJ mol^{-1}) and Mn—O (402 kJ mol^{-1}), which enhances structural stability by reducing the TM—O bond lengths.[24–26,30] XRD refinement confirms a contraction of TM—O bond length from 2.0542 Å in NFMO to 2.0434 Å in NFMTO, attributable to the substitution of smaller, more highly charged Ti^{4+} ions into the transition-metal sites. Consistent with this densification, the unit cell volume decreases from 128.30 Å^3; in NFMO to 125.73 Å^3; in NFMTO, producing a more compact

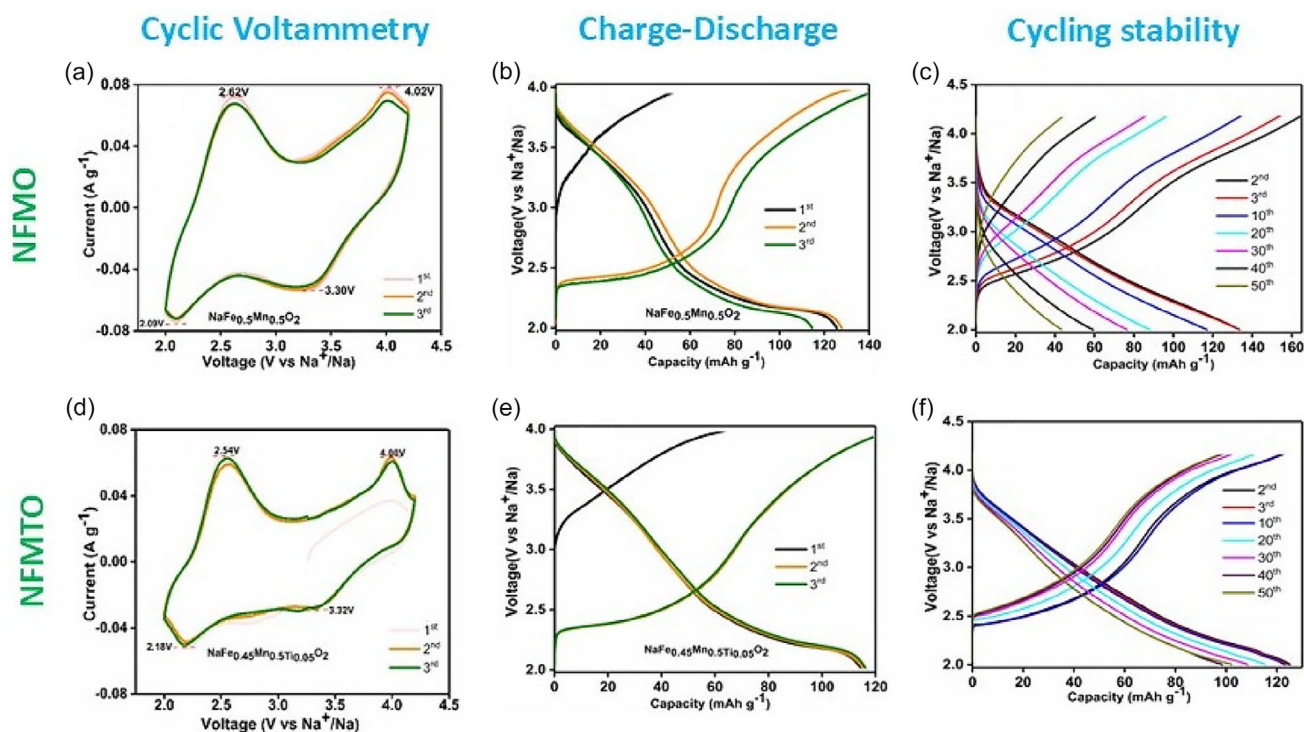**Figure 3.** Electrochemical performance of NFMO and NFMTO half-cells. a,d) CV profiles in the voltage range of 2.0–4.2 V at a scan rate of 0.1 mV/s; b,e) GCD curves at a 0.1C rate for initial 3 cycles in the 2.0–4.0 V range; and c,f) cycling stability upto 50 cycles at a 0.1C rate in the 2.0–4.2 V range.
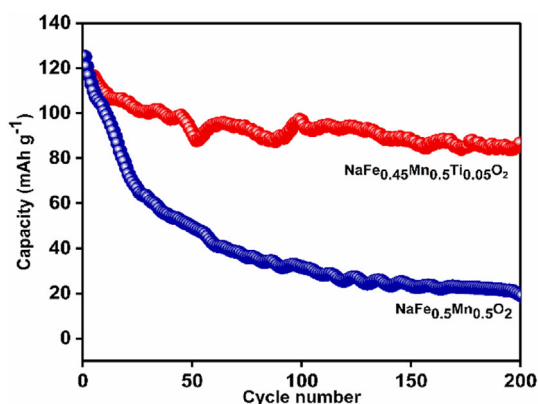
Batteries & Supercaps

Research Article
doi.org/10.1002/batt.202500498

Chemistry Europe
European Chemical
Societies Publishing

Figure 4. Discharge capacity of NFMO and NFMTO half-cells for 200 cycles at 0.1C rate.

lattice with stronger TM—O interactions. Such structural tightening mitigates mechanical strain during Na^+ insertion/extraction, thereby enhancing cycling stability and suppressing phase transitions.[31]

In addition, previous studies by Cao et al. and Chao et al. demonstrated that Ti^{4+} doping suppresses lattice oxygen loss associated with irreversible oxygen redox activity, owing to the higher Ti—O bond energy relative to other transition metal–oxygen bonds, further reinforcing the framework and improving structural stability.[32,33]

Moreover, the presence of tetravalent manganese (Mn^{4+}), is well known to act as a structural stabilizer in cathode materials, thereby improving cycling performance. XPS analysis confirms a decrease in Mn^{3+} content in NFMTO compared to pristine NFMO, indicating suppression of the Jahn–Teller distortion. Similar trends were reported by Shuangwu Xu et al. for O3-type layered cathode materials.[34]

To evaluate the practical applicability of the full cell, a pouch cell with an N/P ratio of 1.08 was assembled, delivering a higher initial discharge capacity of 103 mAh g^{-1} at 0.05C and retaining 90% of its capacity after 10 cycles, as shown in **Figure 5**.
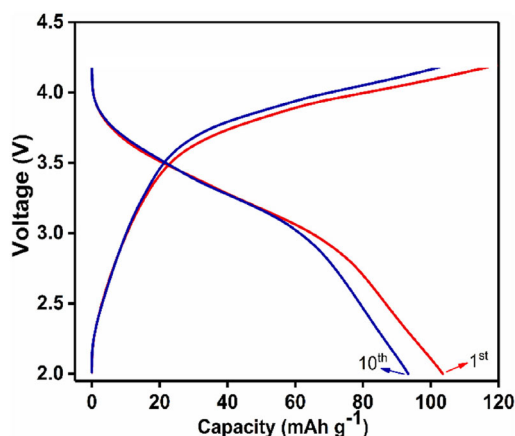

Figure 5. Charge–discharge curves of the NFMTO pouch cell in the voltage window of 2.0–4.2 V at a 0.05 C rate.

3. Conclusion

A cobalt- and nickel-free layered oxide cathode, $NaFe_{0.45}Mn_{0.5}Ti_{0.05}O_2$ (NFMTO), has been developed for SIBs, addressing key challenges related to material sustainability and cost without compromising electrochemical performance. Strategic Ti^{4+} doping within the Fe/Mn lattice significantly enhanced the structural robustness and cycling stability of the material. The NFMTO cathode delivered an initial discharge capacity of 125 mAh g^{-1} within a voltage range of 2.0–4.2 V at 0.1C, maintaining 78.4% capacity retention after 50 cycles. Notably, stable long-term cycling was achieved within 2.0–4.0 V, with 118 mAh g^{-1} and 70% retention over 200 cycles. The practical viability of NFMTO was further demonstrated through pouch cell assembly, underscoring its potential as a high-performance and sustainable cathode material for SIBs.

4. Experimental Section

Material Synthesis

The layered oxide materials $NaFe_{0.5}Mn_{0.5}O_2$ (NFMO) and $NaFe_{0.45}Mn_{0.5}Ti_{0.05}O_2$ (NFMTO) were synthesized via a solid-state method using stoichiometric amounts of sodium carbonate (Na_2CO_3, Sigma Aldrich, 99.5%), iron (III) oxide (Fe_2O_3, Alfa Aesar, 95.0%), manganese (III) oxide (Mn_2O_3, Sigma Aldrich, 99%), and titanium (IV) oxide (TiO_2, Aldrich, 99%). To compensate for potential sodium loss during the high-temperature synthesis, a 5% molar excess of Na_2CO_3 was included in the precursor mixture. In a typical synthesis, a 5 g batch of the precursor mixture was ball-milled in isopropyl alcohol (IPA) for 6 h. The resulting powder was then calcined at 900 °C in air for 12 h. After cooling to room temperature, the obtained samples were stored in an argon-filled glovebox to prevent air exposure.

Materials Characterization

The XRD patterns of the prepared samples were obtained using a Bruker D8 Advance diffractometer with a Cu K$_\alpha$ radiation source ($\lambda = 1.5416$ Å). The resulting diffraction patterns were subjected to Rietveld refinement using GSAS software to obtain the crystal structure and lattice parameters. The surface morphology of the samples was investigated via FESEM on a TESCAN MIRA-3 LMU instrument. High resolution transmission electron microscopy (HRTEM) studies were performed using a Thermo Scientific Talos F200S to further elucidate the microstructure. The surface elemental composition and chemical states were analyzed using XPS on a Thermo Fisher Scientific MultiLab 2000 spectrometer, utilizing nonmonochromatic Al K$_\alpha$ radiation (1486.6 eV).

Electrochemical Analyses

Electrochemical tests were conducted in Swagelok-type Na-metal half-cells, using metallic sodium as the counter electrode. The composite positive electrode was prepared by thoroughly mixing and grinding layered oxides with Super P carbon (70:30 weight ratio) in an agate mortar for 30 min. The cells were cycled at a 0.1C rate within a voltage window of 2.0–4.0 V (also up to 4.2V) versus Na$^+$/Na using a Bio-Logic cycler. For full-cell studies, a negative electrode was prepared using hard carbon (Kuraray Type-1) and coated on Cu

Batteries & Supercaps

Research Article
doi.org/10.1002/batt.202500498

Chemistry Europe
European Chemical
Societies Publishing

foil (16 mm, 1.59 mg cm^{-2} loading, dried at 80 °C for 12 h under vacuum). The positive electrode was prepared by coating a slurry (70 wt% active material, 20 wt% Super P carbon, and 10 wt% PVDF binder in N-Methyl-2-pyrrolidone onto Al foil and dried at 80 °C for 12 hr under vacuum. Coin cells were assembled in an Ar-filled glovebox, while the pouch cell of dimension 6.5 x 4.5 cm was assembled in a dry room (RH < 1%). The 0.5 M of NaPF$_6$ in EC:PC:DEC was used as electrolyte. For the full cell, mass loading was 3.53 mg cm^{-2}, the negative-to-positive (N/P) ratio was 1.08, areal capacity was ≈0.353 mAh cm^{-2}, and electrolyte volume was 30 μL cm^{-2}.

Acknowledgements

Conflict of Interest

The authors declare no conflict of interest.

Data Availability Statement

The data that support the findings of this study are available from the corresponding author upon reasonable request.

[1] H. Kim, H. Kim, Z. Ding, M. H. Lee, K. Lim, G. Yoon, K. Kang, *Adv. Energy Mater.* **2016**, *6*, 1600943.

[2] M. Lao, Y. Zhang, W. B. Luo, Q. Yan, W. Sun, S. X. Dou, *Adv. Mater.* **2017**, *29*, 1700622.

[3] J. Deng, W.-B. Luo, S.-L. Chou, H.-K. Liu, S.-X. Dou, *Adv. Energy Mater.* **2017**, *7*, 1701428.

[4] M. Armand, J.-M. Tarascon, *Nature* **2008**, *451*, 652.

[5] K. Lin, J. Chen, C. Lin, L. Liu, G. Zhang, S. Sun, Z. Shi, *Chem. Eng. J.* **2023**, *452*, 138904.

[6] J. Chen, T. Liu, M. Chu, K. Yu, X. Xie, K. Lin, Y. Cheng, X. Zhang, J. Li, Z. Shi, *J. Mater. Chem. A.* **2024**, *12*, 25222.

[7] Z. Shen, J. Zhu, J. Huang, K. Cao, N. Wang, Z. Shi, *Mater. Lett.* **2025**, *379*, 137654.

[8] H. Deng, L. Liu, Z. Shi, *Mater. Lett.* **2023**, *340*, 134113.

[9] Y. Yang, H. Deng, L. Liu, J. Pan, P. Chen, Z. Shi, *J. Power Sources* **2024**, *616*, 235082.

[10] Y. X. Lu, X. H. Rong, Y. S. Hu, L. Q. Chen, H. Li, *Energy Storage Mater.* **2019**, *23*, 144.

[11] C. Delmas, C. Fouassier, P. Hagenmuller, *Physica B+C* **1980**, *99*, 81.

[12] Q. Liu, Z. Hu, M. Chen, C. Zou, H. Jin, S. Wang, S.-L. Chou, S.-X. Dou, *Small* **2019**, *15*, 1805381.

[13] C. Delmas, D. Carlier, M. Guignard, *Adv. Energy Mater.* **2020**, *11*, 2001201.

[14] K. Kubota, S. Kumakura, Y. Yoda, K. Kuroki, S. Komaba, *Adv. Energy Mater.* **2018**, *8*, 1703415.

[15] D. Kundu, E. Talaie, V. Duffort, L. F. Nazar, *Angew. Chem. Int. Ed.* **2015**, *54*, 3431.

[16] H. Yoshida, N. Yabuuchi, S. Komaba, *Electrochem. Commun.* **2013**, *34*, 60.

[17] P. Vassilaras, A. J. Toumar, G. Ceder, *Electrochem. Commun.* **2014**, *38*, 79.

[18] Y. Lu, W. Kong, Q. Li, D. Ning, G. Schuck, G. Schumacher, C. Su, X. Liu, *ACS Appl. Energy Mater.* **2020**, *3*, 933.

[19] S. Mariyappan, Q. Wang, J. M. Tarascon, *J. Electrochem. Soc.* **2018**, *165*, A3714.

[20] L. Zheng, M. N. Obrovac, *Electrochim. Acta* **2017**, *233*, 284.

[21] H. Yu, S. Guo, Y. Zhu, M. Ishida, H. Zhou, *Chem. Commun.* **2014**, *50*, 457.

[22] P. F. Wang, H.-R. Yao, X.-Y. Liu, J.-N. Zhang, L. Gu, X.-Q. Yu, Y.-X. Yin, Y.-G. Guo, *Adv. Mater.* **2017**, *29*, 1700210.

[23] M. Sathiya, Q. Jacquet, M.-L. Doublet, O. M. Karakulina, J. Hadermann, J.-M. Tarascon, *Adv. Energy Mater.* **2018**, *8*, 1702599.

[24] Q. Wang, S. Mariyappan, J. Vergnet, A. M. Abakumov, G. Rousse, F. Rabuel, M. Chakir, J. M. Tarascon, *Adv. Energy Mater.* **2019**, *9*, 1901785.

[25] P.-F. Wang, H.-R. Yao, X.-Y. Liu, J.-N. Zhang, L. Gu, X.-Q. Yu, Y.-X. Yin, Y.-G. Guo, *Adv. Mater.* **2017**, *29*, 1700210.

[26] L. Yu, X. X. Xing, S. Y. Zhang, X. Zhang, X. Han, P.-F. Wang, S. Xu, *ACS Appl. Mater. Interfaces* **2021**, *13*, 32948.

[27] S. K. Gogula, V. A. Gangadharappa, V. K. Jayaraman, A. Pavithran, A. S. Prakash, *J. Phys. Chem. C* **2024**, *128*, 2362.

[28] W. Kang, Z. Zhang, P.-K. Lee, T.-W. Ng, W. Li, Y. Tang, W. Zhang, C.-S. Lee, D. Y. W. Yu, *J. Mater. Chem. A.* **2015**, *3*, 22846.

[29] R. J. Clément, J. Billaud, A. R. Armstrong, G. Singh, T. Rojo, P. G. Bruce, C. P. Grey, *Energy Environ. Sci.* **2016**, *9*, 3240.

[30] Y. M. Zheng, X.-B. Huang, X.-M. Meng, S.-D. Xu, L. Chen, S.-B. Liu, D. Zhang, *ACS Appl. Mater. Interfaces* **2021**, *13*, 45528.

[31] V. Gangadharappa, P. Devi, V. K. Jayaraman, U. Anil, P. Murugan, A. S. Prakash, *Batteries & Supercaps* **2025**, *00*, e202500320.

[32] X. Cao, X. Li, Y. Qiao, M. Jia, F. Qiu, Y. He, P. He, H. Zhou, *ACS Energy Lett.* **2019**, *4*, 2409.

[33] C. Li, C. Zhao, B. Hu, B. Wong, M. Shen, B. Hu, *Chem. Mater.* **2020**, *32*, 1054.

[34] S. Xu, H. Chen, C. Li, R. Nie, Y. Yang, M. Zhou, X. Zhang, H. Zhou, *J. Alloys Compd.* **2023**, *962*, 171199.